

Massive protostars as gamma-ray sources

V. Bosch-Ramon¹, G. E. Romero^{2,3,*}, A. T. Araudo^{2,3}, and J. M. Paredes¹

¹ Departament d’Astronomia i Meteorologia and Institut de Ciències del Cosmos (ICC), Universitat de Barcelona (UB/IEEC), Martí i Franquès 1, 08028, Barcelona, Spain

² Instituto Argentino de Radioastronomía (CCT La Plata, CONICET), C.C.5, (1894) Villa Elisa, Buenos Aires, Argentina

³ Facultad de Ciencias Astronómicas y Geofísicas, Universidad Nacional de La Plata, Paseo del Bosque, 1900 La Plata, Argentina

Received / Accepted

ABSTRACT

Context. Massive protostars have associated bipolar outflows with velocities of hundreds of km s^{-1} . Such outflows can produce strong shocks when interact with the ambient medium leading to regions of non-thermal radio emission.

Aims. We aim at exploring under which conditions relativistic particles are accelerated at the terminal shocks of the protostellar jets and can produce significant gamma-ray emission.

Methods. We estimate the conditions necessary for particle acceleration up to very high energies and gamma-ray production in the non-thermal hot spots of jets associated with massive protostars embedded in dense molecular clouds.

Results. We show that relativistic Bremsstrahlung and proton-proton collisions can make molecular clouds with massive young stellar objects detectable by the *Fermi* satellite at MeV-GeV energies and by Cherenkov telescope arrays in the GeV-TeV range.

Conclusions. Gamma-ray astronomy can be used to probe the physical conditions in star forming regions and particle acceleration processes in the complex environment of massive molecular clouds.

Key words. Stars: formation–gamma-rays: theory–stars: early-type –ISM: clouds

1. Introduction

Massive stars are formed in the dense cores of massive cold clouds (Garay & Lizano 1999, and references therein). The accumulation of gas in the core might proceed through previous stages of fragmentation and coalescence with the progressive result of a massive protostar that then accretes from the environment (e.g. Bonnell et al. 1997, Stahler et al. 2000) or through direct accretion onto a central object of very high mass (e.g. Rodríguez et al. 2008 -RMF08-; see Shu et al. 1987 for the basic mechanism). In any case, the prestellar core is expected to have angular momentum, which would lead to the formation of an accretion disk. The strong magnetic fields inside the cloud that thread the disk should be pulled toward the protostar and twisted by the rotation giving rise to a magnetic tower, with the consequent outflows, as shown by numerical simulations (e.g. Banerjee & Pudritz 2006, 2007).

Evidence of molecular outflows is found through methanol masers, which are likely associated with shocks formed by the interaction with the external medium (e.g. Plambeck & Menten 1990). However, the most important evidence for outflows comes from the detection of thermal radio jets. These jets are observed to propagate through the cloud material along distances of a fraction of a parsec (e.g. Martí et al. 1993 -MRR93-). At the end point

of the jets, hot spots due to the terminal shocks are observed in several sources. In a few cases, these hot spots are clearly non-thermal, indicating the presence of relativistic electrons that produce synchrotron radiation (e.g. Araudo et al. 2007 -ARA07-, 2008).

A population of relativistic electrons in the complex environment of the massive molecular cloud in which the protostar is being formed will produce high-energy radiation through a variety of processes: inverse Compton (IC) scattering of infrared (IR) photons from the cloud, relativistic Bremsstrahlung, and, if protons are accelerated at the shock as well, inelastic proton-proton (*pp*) collisions. If such radiation is detectable, gamma-ray astronomy can be used to shed light on the star forming process, the protostar environment, and cosmic ray acceleration inside molecular clouds.

This work is devoted to discuss under what conditions the terminal shocks of jets from massive protostars can efficiently accelerate particles, and produce gamma rays that may be detectable by the *Fermi* satellite and Cherenkov telescopes in the near future. The model developed for the calculations is essentially different from the phenomenologic model presented by ARA07, since now the dynamics of the jet termination region is characterized, the shock power estimated, the conditions for particle acceleration analyzed, and the role of hydrodynamical instabilities for non-thermal radiation explored. In short, the acceleration and emission are consistently modeled together with the hydrodynamics in a more physical scenario. Our study is

Send offprint requests to: V. Bosch-Ramon:
vbosch@mpi-hd.mpg.de

* Member of CONICET, Argentina

partially based on early works on non-thermal emission in young stellar objects (YSO), as those by Crusius-Watzel (1990) and Henriksen et al. (1991), but we develop further some important aspects of the hydrodynamics-radiation relation, and focus on massive YSOs and the feasibility of their detection with the present observational facilities.

2. Physical scenario

A massive YSO, or a group of them, are deeply embedded into a molecular cloud. The protostar heats the cloud in such a way that it can be detected as a strong IR source, with luminosities in the range $L_{\text{IR}} \sim 10^{4-5} L_{\odot} \sim 10^{38-39} \text{ erg s}^{-1}$, whereas the optical counterpart is obscured by the cloud. Masses and sizes of these clouds are of the order of $\sim 10^3 M_{\odot}$ and few pc, respectively (e.g. Garay & Lizano 1999), and the densities in the regions in which the massive YSOs are found typically span $n_c \sim 10^3 - 10^6 \text{ cm}^{-3}$ (see Araudo et al. 2008 and references therein).

As already mentioned, collimated outflows are present in most of massive YSOs, and thermal radiation have been detected up to distances of $10^{16} - 10^{18} \text{ cm}$ from the central star. These jets have temperatures of $\sim 10^4 \text{ K}$ and move at speeds (v_j) from several hundreds to $\sim 1000 \text{ km s}^{-1}$ (e.g. MRR93, Martí, Rodríguez and Reipurth 1995 -MRR95-). This shows that they are strongly supersonic flows with Mach numbers $M \gtrsim 10$. The kinetic luminosities of these jets are expected to be $L_j \sim 10^{36} \text{ erg s}^{-1}$ (e.g. MRR95, ARA07).

In some cases (see Araudo et al. 2008), non-thermal radio lobes have been detected at distances of $Z_j \sim \text{pc}$, with sizes of $\sim 1\%$ of this distance (MRR93, Garay et al. 2003 -GAR03-). Given the directions, sizes and distances from the core, the lobes are compatible with being produced by the head of the jet. These radio lobes are likely generated by the strong terminal shocks of the jets, which also ionize the shocked material. Magnetic fields should also be present, since they play an important role supporting the cloud before the gravitational collapse, allowing the required high densities in the cores to be achieved (e.g. McKee & Ostriker 2007). Estimates from Zeeman measurements of the cloud magnetic field give values $B_c \sim 0.3n_{c5}^{1/2} \text{ mG}$ (e.g. Crutcher 1999), where $n_{c5} = n_c/(10^5 \text{ cm}^{-3})$ is the cloud density. Under these conditions, particles can be accelerated up to relativistic energies via diffusive shock (Fermi I) acceleration (DSA, e.g. Bell 1978; see Drury 1983 for a review). These particles would produce the radiation of non-thermal nature found in the lobes, and could generate significant emission in a broad spectral range, from radio to gamma rays.

Some amount of thermal ultraviolet (UV)/X-ray photons is expected from the shocked material. This radiation will suffer strong photo-electric absorption in the regions of the cloud next to the jet head and will ionize the surrounding material improving the conditions for efficient particle acceleration (e.g. Drury et al. 1996). On the other hand, fast radiative cooling of the shocked material can affect the lobe dynamics, and also reduce the efficiency of DSA, but could increase the detectability of massive YSO at high energies because of the density enhancement. Finally, ionization losses of radio emitting electrons and free-free absorption by the ionized medium could affect significantly

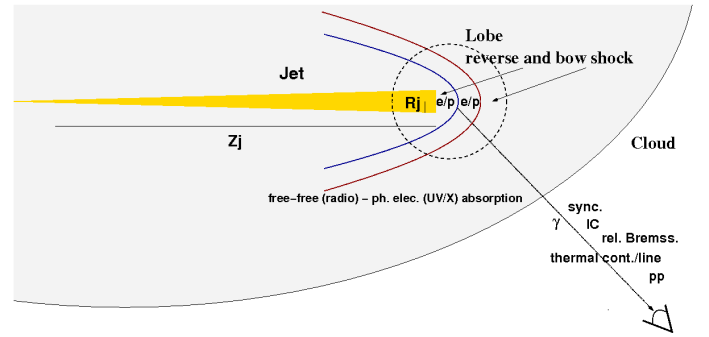


Fig. 1. Sketch of the termination region of the jet of a massive YSO. Two shocks of different strengths and velocities, depending on the jet-medium properties, will form. Electrons and protons can be accelerated in the shocks, and generate non-thermal emission via interaction with the ambient matter, magnetic and radiation fields. The shocked material will also produce thermal radiation.

the radio spectrum. In some sources, free-free emission may dominate the radio band.

In Fig. 1 we sketch the scenario in which non-thermal emission is produced through the acceleration of electrons and protons in the jet termination regions.

3. On the physical nature of the lobes

We assume that the non-thermal radio lobes are the regions in which the protostellar jets terminate. The action of the jet head on the external medium leads to two shocks, one moving in the cloud material and another one in the jet itself; these are the bow shock and the reverse shock, respectively. These shocks would be the accelerators of the relativistic particles generating the observed non-thermal radio emission.

3.1. Dynamics of the jet termination shocks

An important parameter determining the shock characteristics is the jet (j) to cloud (c) density ratio $\chi = n_j/n_c$. For fiducial values of the jet properties, say $v_j \sim 10^8 \text{ cm s}^{-1}$, $L_j \sim 10^{36} \text{ erg s}^{-1}$ and jet radius $R_j \sim 10^{16} - 10^{17} \text{ cm}$ (assuming that lobe and jet radii are similar), we obtain jet densities in the range $n_j \sim 10^2 - 10^4 \text{ cm}^{-3}$ at the location of the lobe; then, $\chi \sim 10^{-4} - 10$.

The value of χ , together with v_j , determines the speed of the bow shock (e.g. Blondin et al. 1989):

$$\begin{aligned} v_{\text{bs}} &\approx (1 + \chi^{-1/2})^{-1} v_j \approx (0.01 - 0.8) v_j \\ &\approx 10^6 - 10^8 v_{\text{js}} \text{ cm s}^{-1}, \end{aligned} \quad (1)$$

where $v_{\text{js}} = v_j/(10^8 \text{ cm s}^{-1})$. The reverse shock velocity is $v_r \sim v_j - 3/4 v_{\text{bs}}$. The life time of the jet, which can be written as $t_{\text{life}} \approx Z_j/v_{\text{bs}}$, can be also expressed as a function of v_{js} and the parameters $Z_{\text{pc}} = Z_j/(1 \text{ pc})$, $\chi_{0.1} = \chi/0.1$:

$$t_{\text{life}} \approx Z_j/v_{\text{bs}} \sim 3 \times 10^{10} Z_{\text{pc}} v_{\text{js}}^{-1} \text{ s}, \quad \text{when } \chi > 1, \quad (2)$$

and

$$t_{\text{life}} \approx Z_j/v_{\text{bs}} \approx 10^{11} Z_{\text{pc}} v_{\text{js}}^{-1} \chi_{0.1}^{-1/2} \text{ s}, \quad \text{when } \chi < 1. \quad (3)$$

Equations 2 and 3 show that the jet advance takes place in two different regimes depending on the jet-medium density ratio, which depends in turn on the source age. As long as the jet lateral pressure is larger than that of the surrounding medium, the jet expands freely and thereby $n_j \propto R_j^2 \propto Z_j^2$, i.e. the jet has a conical shape. For very young jets, when $\chi > 1$, the advancing jet head speed is constant ($v_{\text{bs}} \sim v_j$), and therefore the jet lifetime is simply $t \propto Z_j$. However, the jet head gets diluted. Since $\chi \propto Z_j^{-2}$, at some stage $\chi < 1$ and t becomes $\propto Z_j^2$. This Z_j - t dependence implies that most of the sources will be observed when $\chi < 1$.

At some point, the jet expansion is stopped by the external pressure and the jet density becomes roughly constant. When it happens depends on the shocked jet material pressure away from the reverse shock, but it is expected that $\chi \ll 1$. If values as low as $\chi \sim 10^{-4}$ are reached the bow shock will move with a speed below the Alfvén speed (v_A) in the cloud and will not be a shock anymore.

The luminosity crossing the shock surface in the jet and the cloud (reverse and bow shock, respectively) is:

$$L_s = (\pi/2) R_j^2 m_p n_{j,c} v_{r,\text{bs}}^3 \sim 3 \times 10^{35} R_{16}^2 n_{j,c3} v_{r,\text{bs}8}^3 \text{ erg s}^{-1}, \quad (4)$$

where $n_{j,c3} = n_{j,c}/(10^3 \text{ cm}^{-3})$ and $v_{r,\text{bs}8} = v_{r,\text{bs}}/(10^8 \text{ cm s}^{-1})$. The sum of L_s from both shocks cannot be larger than L_j .

When $\chi < 1$, the reverse shock to bow shock luminosity ratio is $\sim \chi^{-1/2}$. This fact, together with the Z_j - t dependence mentioned above, implies that most of the time the reverse shock will be more powerful than the bow shock. On the other hand, for $\chi \gg 1$ the reverse shock will be very weak and the bow shock radiation very faint. Therefore, lobe detection is favored when the jet has expanded enough to reach $\chi \lesssim 1$, being the reverse shock the best place for particle acceleration unless $\chi \sim 1$, when both shocks have similar properties.

3.2. The postshock regions

For purely adiabatic jet-medium interactions, the formation of the reverse shock is accompanied by a strong widening of the jet termination region as in extragalactic FR II sources (e.g. Kaiser & Alexander 1997) and possibly also in microquasars (e.g. Bordas et al. 2009). However, the conditions in massive YSOs are likely different. As noted by Blondin et al. (1989), if the cooling length l_{cool} of the shocked material in either the reverse, the bow shock, or in both, is $< R_j$, the jet head will not expand significantly. Using the cooling function $C(T) \sim 7 \times 10^{-19} T^{-0.6}$ (e.g. Myasnikov et al. 1998) at the temperatures relevant here, adopting a density and speed downstream right after the shock of $4n_{j,c}$ and $v_{r,\text{bs}}/4$, respectively (strong, non-relativistic and lowly magnetized shock), and assuming full ionization in that region, l_{cool} is:

$$l_{\text{cool}} \sim \frac{3kT v_{r,\text{bs}}}{32 n_{j,c} C(T)} \sim 10^{18} v_{r,\text{bs}8}^{4.2} n_{j,c3}^{-1} \text{ cm}. \quad (5)$$

Despite a specific-case treatment and detailed simulations would be required to characterize the fine evolution of the jet head, there is a wide range of realistic parameters for

which the bow shock, and even the reverse shock, can be radiative. This is compatible with the relatively small size of non-thermal radio lobes (see Sect. 2). In case one or both shocks are not radiative, the material cools through adiabatic expansion farther than R_j from the shock. The adiabatic cooling timescale is similar to the advection (or escape) time of the material in the downstream region:

$$t_{\text{esc}} \sim 4 R_j / v_{r,\text{bs}} = 4 \times 10^8 R_{j16} v_{r,\text{bs}8}^{-1} \text{ s}. \quad (6)$$

Because of radiative cooling, the compression ratio Λ , or downstream to upstream density ratio, will grow with the distance downstream from $\Lambda = 4$ to $\sim 3 \times 10^3 v_{\text{ss}}^2$, or to $\sim 20 v_{\text{ss}}^{1/2} n_{j,c3} B_{-3}^{-1}$. The former upper limit for Λ comes from the fact that the temperature stops falling around $T \sim 10^4$ K, and the latter from the enhancement of the magnetic field ($B = 10^{-3} B_{-3}$ G) pressure, which limits the compression (see Blondin et al. 1989).

When $\chi < 1$, the material downstream is $1/\chi$ to $\Lambda_{\text{bs}}/\chi\Lambda_r$ times denser in the bow shock than in the reverse shock. Since a force is exerted by the downstream material of the reverse shock on that of the bow shock, Rayleigh-Taylor (RT) instabilities in the contact discontinuity between both shocks can develop. This phenomenon will distort the jet head on a timescale:

$$t_{\text{RT}} \sim R_j / \chi^{1/2} v_r \sim 3 \times 10^9 R_{j16} \chi_{0.001}^{-1/2} v_{j8}^{-1} \text{ s}, \quad (7)$$

where $\chi'_{0.001} = (\chi\Lambda_r/\Lambda_{\text{bs}})/0.001$ is the effective density jump in the contact discontinuity. Therefore, for $t_{\text{life}} > t_{\text{RT}}$, complex shock structures should form (Blondin et al. 1989) accompanied by strong mixing of material from both shocks. This mixing can lead to an increase of the effective density downstream the reverse shock. To account for this, we have simply parameterized the density downstream the reverse shock as $4n_j < 4Fn_j < \Lambda_{\text{bs}} n_c$, where F is a free parameter that says how much the density departs from the adiabatic value, $4n_j$. Downstream the bow shock, mixing should not affect significantly the density, and hence $F \sim 1$.

Concerning the dynamic role of the jet and cloud magnetic fields at the jet termination region, B_j and B_c , respectively, we will assume hereafter that they are negligible. This applies as long as $B_{j,c} \ll B_{\text{eq}}$, where:

$$B_{\text{eq}} = 30 L_{j36}^{1/2} R_{j16}^{-1} v_{j8}^{-1/2} \text{ mG} \quad (8)$$

is the magnetic field of equipartition between the magnetic and the jet kinetic energy density. If $B_{j,c} \ll B_{\text{eq}}$, it is also expected that the magnetic field in the shock regions, B , should be well below B_{eq}^1 .

4. Particle acceleration in the lobes

4.1. Acceleration and cooling processes

The energies and luminosities that non-thermal particles may achieve depend on the efficiency of particle acceleration, which depends in turn on the lobe properties. As noted above, DSA can operate in the fast strong shocks at the termination of the jets accelerating particles up to relativistic energies. For a parallel, lowly magnetized (i.e.

¹ Note that B_{eq} relates to the jet kinetic energy density, not to the one of the (unshocked) cloud. In the latter, the magnetic field may be indeed dynamically more important.

$v_{r,bs} \gg v_A$ upstream), non-relativistic strong shock, in the test particle approximation and with diffusion coefficient D , the acceleration rate is (e.g. Protheroe 1999):

$$\begin{aligned} \dot{E}_{e,p \text{ gain}} &= \frac{3}{20} d^{-1} \left(\frac{v_{r,bs}}{c} \right)^2 q B c \\ &\approx 1.5 \times 10^{-5} d^{-1} v_{r,bs}^2 B_{-3} \text{ GeV s}^{-1}, \end{aligned} \quad (9)$$

where e and p stand for electrons and protons, respectively, and $d = D/D_B$, with $D_B = cr_g/3$ being the diffusion coefficient in the Bohm limit ($r_g = E/qB$ is the gyroradius of a particle with energy E). The acceleration timescale can be written as:

$$t_{\text{gain}} = E/\dot{E}_{e,p \text{ gain}} \approx 6.7 \times 10^4 d v_{r,bs}^{-2} B_{-3}^{-1} E_{\text{GeV}} \text{ s}, \quad (10)$$

where $E_{\text{GeV}} = E/(1 \text{ GeV})$.

At the maximum energy of particles, t_{gain} becomes equal to the shortest timescales among synchrotron, IC (Thomson regime) and relativistic Bremsstrahlung losses for electrons (see Blumenthal & Gould 1970), inelastic pp collision losses for protons (see Kelner et al. 2006), and diffusive particle escape and jet life time for both electrons and protons. The relevant loss timescales, $t_{\text{loss}} = -E/\dot{E}_{\text{loss}}$, are given by the following expressions:

$$t_{\text{sync}} \approx 4 \times 10^{11} B_{-3}^{-2} E_{\text{GeV}}^{-1} \text{ s}, \quad (11)$$

$$t_{\text{IC}} \approx 1.6 \times 10^{13} u_{\text{IR}-9}^{-1} E_{\text{GeV}}^{-1} \text{ s}, \quad (12)$$

$$t_{\text{Brems}} \approx 3.5 \times 10^{10} n_{j,c3}^{-1} F_{10}^{-1} \text{ s}, \quad (13)$$

$$t_{pp} \approx 5 \times 10^{10} n_{j,c3}^{-1} F_{10}^{-1} \text{ s}, \quad (14)$$

$$t_{\text{diff}} \approx 1.5 \times 10^{12} d^{-1} R_{j16}^2 B_{-3} E_{\text{GeV}}^{-1} \text{ s}, \quad (15)$$

$$t_{\text{life}} \approx 10^{11} Z_{\text{pc}} v_{\text{bs8}}^{-1} \text{ s}, \quad (16)$$

where $u_{\text{IR}-9} = u_{\text{IR}}/10^{-9} \text{ erg cm}^{-3}$ is the energy density of the IR photon field and $F_{10} = F/10$ (recall $F_{10}=0.1$ in the bow shock). Concerning the densities, the compression of the material due to the shock is already accounted. Under the adopted assumptions, particles spend on average ~ 4 times longer in the downstream than in the upstream region, and the conditions downstream the shock will determine the particle evolution. Adiabatic cooling is not considered in the accelerating region.

From the timescales presented above, we obtain the following maximum energies depending on the dominant energy loss mechanism and source age:

$$E_{\text{max sync}} \approx 2.4 \times 10^3 d^{-1/2} v_{r,bs8} B_{-3}^{-1/2} \text{ GeV}, \quad (17)$$

$$E_{\text{max IC}} \approx 1.5 \times 10^4 d^{-1/2} v_{r,bs8} u_{\text{IR}-9}^{-1/2} B_{-3}^{1/2} \text{ GeV}, \quad (18)$$

$$E_{\text{max Brems}} \approx 5.2 \times 10^5 d^{-1} v_{r,bs8}^2 B_{-3} n_{j/c3}^{-1} F_{10}^{-1} \text{ GeV}, \quad (19)$$

$$E_{\text{max pp}} \approx 7.5 \times 10^5 d^{-1} v_{r,bs8}^2 B_{-3} n_{j/c3}^{-1} F_{10}^{-1} \text{ GeV}, \quad (20)$$

$$E_{\text{max diff}} \approx 4.7 \times 10^3 d^{-1} v_{r,bs8} B_{-3} R_{j16} \text{ GeV}, \quad (21)$$

$$E_{\text{max life}} \approx 1.5 \times 10^5 d^{-1} Z_{\text{pc}} v_{r,bs8} B_{-3} \text{ GeV}, \quad (22)$$

This shows that, if $d \sim 1$, electrons and protons can reach very high energies. It turns out that synchrotron and diffusive escape are the dominant mechanisms to limit acceleration, although relativistic Bremsstrahlung and pp collisions can dominate for large densities. We notice that in radiative shocks, R_j should be substituted by l_{cool} in Eqs. (16) and (22).

We note that the accelerated proton to electron number ratio a cannot be established from first principles. It is considered here as a phenomenologic parameter.

4.2. Required conditions for efficient DSA

In DSA particles are scattered by magnetic inhomogeneities back to the shock before escaping downstream/upstream. These inhomogeneities should not move faster than the shock itself, since otherwise the particles would not be affected by the shock velocity jump. If it were the case, stochastic Fermi II particle acceleration could be at work (Fermi 1949). However, in that case most of the jet kinetic energy will not be available and little energy will go to non-thermal particles. Therefore, efficient particle acceleration requires the shock to be super-Alfvénic in the upstream region, i.e. $v_A \ll v_{r,bs}$, where:

$$v_A \approx \sqrt{\frac{B^2}{4\pi X_i n_{j,c} m_p}} \approx 2.1 \times 10^7 B_{-3} X_{i0.1}^{-1/2} n_{j,c3}^{-1/2} \text{ cm s}^{-1}, \quad (23)$$

and $X_i = 0.1 X_{i0.1}$ is the ratio of ionized to total density. Thus, X_i should not be too low.

Downstream the shock, the material is likely ionized through particle collisions, and the magnetic field is expected to be quite disordered. Upstream the shock, UV/X-ray radiation produced in the shock region can photo-ionize the medium unless $v_{bs} \lesssim 10^7 \text{ cm s}^{-1}$ (or $\chi \lesssim 0.01 v_{j8}^{-2}$), since then photons cannot ionize hydrogen. From the recombination and photo-ionization timescales, $t_{\text{re}} \sim 10^{11} X_{i0.1}^{-1} n_{j,c3}^{-1} \text{ s}$ and $t_{\text{ph}} \sim 10^7 R_{16}^2 v_{s8}^2 L_{35}^{-1} \text{ s}$, respectively (the recombination rate and ionization cross section are given in Seaton 1959 and Morrison & McCammon 1983; L_{35} corresponds here to the ionizing photon field luminosity), it seems likely that upstream the shock $t_{\text{ph}} < t_{\text{re}}$, and therefore $X_i \rightarrow 1$. In the radiative regions downstream the shock, X_i may become much smaller than 1.

As noted, the magnetic field should have some level of inhomogeneity: the scattering centers that isotropise particles in both sides of the shock. Magnetic inhomogeneities can develop upstream due to relativistic particle streaming (e.g. Lucek & Bell 2000), but they should not be suppressed by wave damping (see Reville et al. 2007). These inhomogeneities would be advected downstream the shock, thus they would be also present there.

For very high densities, Coulombian/ionization energy losses should not suppress acceleration from suprathermal energies (e.g. Drury et al. 1996). For that, the following condition should be provided:

$$t_{\text{ion}} \sim 3 \times 10^{11} (m_{p,e}/m_e) E_{\text{GeV}} n_{j,c3}^{-1} F_{10}^{-1} \text{ s} > t_{\text{gain}}, \quad (24)$$

which implies:

$$n_{j,c} < 4 \times 10^9 (m_{p,e}/m_e) F_{10}^{-1} v_{s8}^2 B_{-3} \text{ cm}^{-3}. \quad (25)$$

The detection of radio emission from electrons with energy:

$$E \approx 0.6 \nu_5^{1/2} B_{-3}^{-1/2} \text{ GeV} \gg 0.511 \text{ MeV}, \quad (26)$$

where ν is the radiation frequency ($\nu_5 \text{ GHz} = \nu/(5 \text{ GHz})$), is evidence for efficient particle acceleration and hence some degree of ionization and B -inhomogeneity at least in some sources. However, d , which relates to the B -inhomogeneity, may be small or even energy dependent, not allowing particle acceleration to be efficient beyond energies at which electrons produce synchrotron radio emission. Also, if $l_{\text{cool}} \ll R_j$ or mixing were very efficient (large F), electron acceleration could also stop at radio emitting energies because of large densities and strong relativistic Bremsstrahlung losses. In such a case, protons could not reach very high energies neither due to strong pp cooling.

5. Non-thermal emission in the lobes

5.1. The fate of accelerated particles

The electrons and protons accelerated by DSA have at injection an energy spectrum $Q(E) \propto E^{-\Gamma}$ up to E_{max} , with $\Gamma \sim 2$ (e.g. Drury 1983) and total luminosity $L_{\text{nt}}^{e,p} < L_s$. They mainly accumulate downstream the shock, in a region that here will be considered homogeneous and with a typical size $\sim R_j$. When protons are present, secondary electrons and positrons (e^\pm) are injected with almost a power-law in energy in the region in which these protons interact significantly. The injection luminosity and the maximum effective energy of e^\pm will be about a half of the luminosity going to π^0 -decay gamma-rays and ~ 0.1 the energy of protons, respectively (see Kelner et al. 2006). All these particles evolve under the downstream magnetic, matter and radiation fields, losing energy in the form of synchrotron radiation, relativistic Bremsstrahlung and IC emission in the case of electrons, and high-energy photons, neutrinos, e^\pm and other secondary particles via pp collisions in the case of protons.

Only the radiation from the region closer than R_j from the shock will be computed. At distances larger than R_j , particles cool through adiabatic losses due to the re-expansion of the shocked material, producing scarce emission. If densities are large enough (i.e. strongly radiative shocks, $F \gg 1$), electrons will cool fast via ionization/Coulombian losses and relativistic Bremsstrahlung, and protons through pp collisions, and they will not reach the adiabatic cooling region far downstream.

Far upstream the bow shock, particles with t_{diff} shorter than the dominant cooling timescale t_{loss} could escape into the cloud. Some of the highest energy electrons and protons would escape from the accelerator in this way.

The particle distribution, $N(E, t)$, can be obtained solving the transport equation (e.g. Ginzburg & Syrovatskii 1964):

$$\frac{\partial N(t, E)}{\partial t} + \frac{\partial [b(E)N(t, E)]}{\partial E} + \frac{N(t, E)}{t_{\text{esc}}} = Q(E), \quad (27)$$

where $Q(E)$ is assumed to be constant in time and $b(E)$ includes all the cooling rates $-E/t_{\text{loss}}$ relevant for $N(E, t)$, i.e. synchrotron, relativistic Bremsstrahlung and IC processes for electrons and pp collisions for protons. The adiabatic cooling, which would operate far from the shock

as described above, is not considered here. The parameter t_{esc} , the escape time, is the advection timescale (see Eq. 6), different from t_{diff} , which was used to compute $E_{\text{max diff}}$. This escape time is the dominant timescale for the removal of particles from the emitting region. Since in general $t_{\text{esc}} \ll t_{\text{life}}$, particles will be in the steady state, i.e. $\partial N(t, E)/\partial t = 0$.

5.2. Radiation luminosities and spectral energy distributions

5.2.1. Luminosities

Adopting an efficiency $f_{\text{nt}}^{e,p} = 0.1 f_{\text{nt}0.1}^{e,p}$ for transferring shock luminosity to non-thermal particles (electrons or protons), where $f_{\text{nt}}^{e,p} < 1$, we get:

$$L_{\text{nt}}^{e,p} = f_{\text{nt}}^{e,p} L_s = 10^{35} f_{\text{nt}0.1}^{e,p} L_{s36} \text{ erg s}^{-1}, \quad (28)$$

where $L_{s36} = L_s/(10^{36} \text{ erg s}^{-1})$. Since particle escape has the dominant dynamical timescale, we can roughly calculate the relativistic Bremsstrahlung and pp photon bolometric luminosities in the lobe:

$$L_{\text{Brems}} \sim 10^{33} f_{\text{nt}0.1}^e F_{10} R_{j16} v_{s8}^{-1} n_{j,c3} L_{s36} \text{ erg s}^{-1}, \quad (29)$$

$$L_{pp} \sim 10^{32} f_{\text{nt}0.1}^p F_{10} R_{j16} v_{s8}^{-1} n_{j,c3} L_{s36} \text{ erg s}^{-1}. \quad (30)$$

These luminosities cannot be higher than L_{nt}^e and $\sim 1/3 L_{\text{nt}}^p$ for relativistic Bremsstrahlung and pp collisions, respectively. These two mechanisms contribute mainly to the high-energy part of the spectrum. Regarding the synchrotron/IC luminosities, in general, when

$$r(E_{\text{max}}) = t_{\text{sync,IC}}/\min[t_{\text{esc}}, t_{\text{Brems}}, t_{\text{IC,sync}}] < 1 : \quad (31)$$

$$L_{\text{sync,IC}} \sim 10^{35} f_{\text{nt}0.1}^e L_{s36} \text{ erg s}^{-1}. \quad (32)$$

Otherwise:

$$L_{\text{sync,IC}} \sim 10^{35} f_{\text{nt}0.1}^e r^{-1} L_{s36} \text{ erg s}^{-1}. \quad (33)$$

The IC luminosities will be a minor component unless $u_{-9} \gg 1$. Synchrotron and IC contribute to the low- and the high-energy parts of the spectrum, respectively. Note that f_{nt}^e and f_{nt}^p may actually be very different in some sources (as inferred from the proton-to-electron number ratio in cosmic rays, i.e. $a \approx 100$, Ginzburg & Syrovatskii 1964).

The highest energy electrons and protons may escape from the lobe and radiate in the cloud, although the corresponding luminosities depend on the escape probability, which is difficult to quantify.

5.2.2. Spectral energy distributions

If synchrotron or IC losses dominate at $E < E_{\text{max}}$ for electrons, there is a break in the particle energy distribution $N(E, t)$ at $E \sim E_b$, in which $t_{\text{sync,IC}}$ becomes the shortest timescale. Above E_b , $N(E, t) \propto E^{-(\Gamma+1)}$, which yields a spectral energy distribution (SED) of the radiation that is $\propto \epsilon^{(2-\Gamma)/2}$ for synchrotron and IC dominance, and $\propto \epsilon^{1-\Gamma}$ for relativistic Bremsstrahlung (ϵ is the photon energy).

For electron energies $E < E_b$, and at any energy for protons, advection, and relativistic Bremsstrahlung or pp collisions, lead to $N(E, t) \propto E^{-\Gamma}$, which yields a SED

$\propto \epsilon^{(3-\Gamma)/2}$ (synchrotron/IC), and $\propto \epsilon^{2-\Gamma}$ (both relativistic Bremsstrahlung and pp collisions). Below $\epsilon \sim m_e c^2 \sim 0.5$ MeV and $\epsilon \sim m_\pi c^2 \sim 140$ MeV, the SEDs of relativistic Bremsstrahlung and pp collisions become roughly $\propto \epsilon$ and $\propto \epsilon^2$, respectively.

Dominant ionization/Coulombian losses, relevant only for electrons in our context, lead to $N(E, t) \propto E^{1-\Gamma}$, yielding a SED $\propto \epsilon^{2-\Gamma/2}$ and $\propto \epsilon^{3-\Gamma}$ for synchrotron/IC and relativistic Bremsstrahlung, respectively.

5.2.3. Requirements from observed spectra

The non-thermal nature of the observed radio spectra in several specific cases implies that strong free-free absorption of radio emission should not occur in the lobe or in the surroundings. Far from the lobe the ionization degree should be small. Close to the lobe, the medium is ionized and it is necessary to account for free-free absorption, which is expected to be large downstream the bow shock. The free-free opacity there can be written as (Rybicki & Lightman 1979):

$$\tau_{\text{ff}} \sim 0.03 T_5^{-1.5} \nu_5^{-2} X_{10.1}^2 n_{c5}^2 \Lambda_{10}^2 l_{16}, \quad (34)$$

where $T_5 = T/10^5$ K, and $l_{16} = l/(10^{16}$ cm) is the typical size of the region. Also, suppression of emission at frequencies $\nu < 2 \times 10^8 n_{j,c5} X_{10.1}/B_{-3}$ Hz, due to the Tsytovich-Razin effect, should be considered.

Another condition that should be fulfilled given the observed radio spectra is that either electron escape or relativistic Bremsstrahlung should dominate over Coulombian/ionization losses at low electron energies, i.e. $\alpha \sim 0.5$ ($F_\nu \propto \nu^{-\alpha}$). From the timescale ratios:

$$t_{\text{ion}}/t_{\text{esc}} \sim 8 \times 10^2 E_{\text{GeV}} n_{j,c3}^{-1} F_{10}^{-1} v_{r,bs8}^{-1} \quad \text{and} \quad (35)$$

$$t_{\text{ion}}/t_{\text{Brems}} \sim 9 E_{\text{GeV}}, \quad (36)$$

it is seen that upstream and downstream the shock, radio emitting electrons are dominated by escape or relativistic Bremsstrahlung losses. Note that sources with spectra harder than $F_\nu \propto \nu^{-0.5}$ may be still explained in a non-thermal scenario by moderate free-free absorption and/or ionization cooling (or a thermal component, see below).

5.3. Deriving the magnetic field strength

Assuming a value for L_{nt}^e , plus some additional simplifying assumptions, a formula has been obtained to derive the magnetic field strength consistent with the observed radio fluxes. Taking the radio fluxes at a certain frequency, a particle energy distribution with $\Gamma \sim 2$ and normalized with the total energy $\sim L_{\text{nt}}^e t_{\text{esc}}$, the synchrotron power for one electron ($\dot{E} \approx 4.1 \times 10^{-15} B_{-3}^2 E_{\text{GeV}}^2 \text{ erg s}^{-1}$), and the reasonable simplification that electrons of energy E produce only photons of frequency $\nu \approx 5 \times 10^9 B_{-3} E_{\text{GeV}}^2$ Hz, we obtain:

$$B \sim 0.04 (L_{\text{nt}35}^e)^{-2/3} R_{j16}^{-2/3} v_{s8}^{2/3} \nu_5^{1/3} d_{3 \text{ kpc}}^{4/3} F_\nu^{2/3} \text{ mG}, \quad (37)$$

where d_{kpc} is the distance the source in kpc, and F_ν mJy the flux in mJy at the relevant frequency. In case the radio emitting leptons are secondary e^\pm , then in Eq. (37) it should be changed:

$$L_{\text{nt}}^e \rightarrow 0.1 (t_{\text{esc}}/t_{pp}) L_{\text{nt}}^p. \quad (38)$$

6. Thermal emission in the lobes

The shocked material is heated up to $T \approx 2.3 \times 10^7 v_{s8}^2$ K ($2.4 v_{s8}^2$ keV) and generates line and thermal Bremsstrahlung continuum emission. The total luminosity cannot overcome L_s , and it might be much smaller if the reverse shock is adiabatic and the bow shock relatively slow. This radiation can be absorbed in the cloud core, since the photo-electric opacity coefficient is $\tau_X \sim 20(\epsilon_{\text{keV}})^{-2.5} N_{\text{H}23}$ (within a factor of 2 in the relevant energy range; see Morrison & McCammon 1983), where $\epsilon_{\text{keV}} = \epsilon/\text{keV}$ is the photon energy and $N_{\text{H}} = 10^{23} N_{\text{H}23} = 10^{23} n_{c5} l_{18} \text{ cm}^{-2}$ the neutral hydrogen column density of the lobe surroundings.

The density in the shock regions should neither be too high, to avoid suppression of the acceleration due to strong cooling, nor too low, to avoid that $v_A \gtrsim v_{r,bs}$. Actually, there is room for the shocks to be radiative, producing thermal X-rays that may escape the cloud, without necessarily suppressing particle acceleration.

The fact that thermal radio emission should not overcome the non-thermal component at the same frequencies put some constraints on the scenario. The thermal SED peaks at energies up to \sim keV and is harder than the synchrotron SED, which should generally peak at lower energies. This means that the total L_{sync} must be $\ll L_s$ ($L_{\text{sync}} \lesssim 10^{-4} L_s$ for $\Gamma = 2$), if the non-thermal radio emission is to be dominated by the thermal one. This condition is hard to fulfill unless $f_{\text{nt}}^e \ll 1$. It is worth noting that a radio spectra harder than $\nu^{-0.5}$ may be non-thermal radiation contaminated by a thermal component.

As mentioned in Sect. 1, several massive YSOs present non-thermal radio emission. Two among the most relevant of them are studied in next section: IRAS 16547–4247 and the complex source HH 80–81.

7. Application to IRAS 16547–4247 North and HH 80

The model described in Sect. 5.1 is applied now to the northern radio lobe of the massive YSO IRAS 16547–4247 (IRAS-N), and to the radio lobe HH 80 in the complex source HH 80–81. Both lobes have a clear non-thermal nature (e.g. GAR03; MRR93). IRAS-N shows also an extended structure pointing to the South-East, and HH 80 has a similar non-thermal source very nearby, HH 81. We will not consider here either the South-East extension of IRAS-N nor HH 81. Note however that the extension in IRAS-N may be in fact a fore/background object (RMF08), and HH 81 could be part of the expected complex structure of the jet termination region (see Sect 3; see also Heathcote et al. 1998 -HRR98- for a detailed optical study of the HH 80–81 complex).

7.1. IRAS-N and HH 80 properties

We focus on IRAS-N and HH 80 because both sources are at the two extremes of the density parameter range presented above. IRAS-N is embedded in a very dense cloud, with $n_c \sim 5 \times 10^5 \text{ cm}^{-3}$ (GAR03), whereas HH 80 is thought to be close to the border of a cloud, in a more diluted medium with $n_c \sim 10^2 - 10^3 \text{ cm}^{-3}$ (e.g. MRR93; HRR98; Pravdo et al. 2004 -PTM04-). The distances to IRAS-N and HH 80 are $d \sim 2.9$ kpc and ~ 1.7 kpc (RMF08; MRR93), and the central stars show luminosities of $L_* \approx 5 \times 10^{38}$ and

8×10^{37} erg s⁻¹, respectively (GAR03; MRR93). This radiation provides the main contribution to the infrared emission in the lobes, yielding photon energy densities there of $u \sim 2 \times 10^{-9}$ erg cm⁻³ for IRAS-N, and 2×10^{-12} erg cm⁻³ for HH 80. The distances from the central star to the lobes are $Z_j \approx 5 \times 10^{17}$ cm for IRAS-N, accounting for a jet inclination angle of 84° (Garay et al. 2007), and $\sim 10^{19}$ cm for HH 80, with a not so well constrained jet inclination (see however HRR98). The lobe sizes for IRAS-N and HH 80 are about $R_j \approx 1.6 \times 10^{16}$ cm and 5×10^{16} cm, (RMF08; MRR93), the velocities of the jets are expected to be around $v_j \sim 5 \times 10^7$ cm s⁻¹ and $\sim 10^8$ cm s⁻¹, and the velocities of the bow shocks would be $v_{bs} < 10^7$ cm s⁻¹ and $\sim 5 \times 10^7$ cm s⁻¹, respectively (RMF08; MRR93, MRR95, HRR98). IRAS-N has not been detected in X-rays (see ARA07), whereas HH 80 has been detected by *XMM* (PTM04).

7.1.1. Derived parameters

The values of v_{bs} for IRAS-N imply that $\chi \lesssim 0.04$ and $v_r \sim v_j$. In fact, from the inferred age of IRAS-N, $t_{life} \sim 10^{11}$ s (Garay et al. 2007), Z_j and v_j , a particle density of $n_j \sim 5 \times 10^3$ cm⁻³ can be derived, i.e. $\chi \sim 0.01$ and $v_{bs} \sim 5 \times 10^6$ cm s⁻¹, consistent with the limit given above. Such a value for n_j , together with R_j and v_j , renders a $L_j \sim 5 \times 10^{35}$ erg s⁻¹ for IRAS-N. Given that $v_r \sim v_j$ in this source, it is the case that $L_s \sim L_j$ in the reverse shock. The bow-shock luminosity will be $\sim 4 \times 10^{34}$ erg s⁻¹.

For HH 80, since $n_c \sim n_j$, then $\chi \sim 1$, and therefore we have that $v_r \sim v_{bs}$. In the case of HH 80 this means that both the reverse shock and the bow shock may contribute to the non-thermal radiation (see also HRR98). Accounting for χ and v_j , it can be inferred $t_{life} \sim 3 \times 10^{11}$ s, not far from the value discussed in MRR93; also, $v_r \sim v_{bs}$. Taking $L_j \sim 2 \times 10^{36}$ erg s⁻¹ (MRR95), we get $n_j \sim 4 \times 10^2$ cm⁻³ and, since $\chi \sim 1$, $n_c \sim 4 \times 10^2$ cm⁻³. This latter value is between those inferred from X-ray and optical observations (see the discussion in PTM04). We will treat the bow shock and the reverse shock in HH 80 as a single physical system, with speed 5×10^7 cm s⁻¹ and $L_s = L_j$. The full list of the relevant properties of IRAS-N and HH 80, together with the derived parameters, is presented in Table 1.

Interestingly, the central star is brighter in IRAS-N than in HH 80, but L_j seems smaller in the former. This could be related to the larger density of the environment in IRAS-N. This may have induced jet deceleration through, e.g., medium mass entrainment in the jet. Nevertheless, the uncertainties are large and no strong conclusions can be derived in this regard.

It is worth mentioning that very powerful, slow molecular outflows with luminosities 10–100 times larger than L_j have been detected in the two sources (see RMF08 and references therein).

7.2. Estimates of the emission in IRAS-N and HH 80

7.2.1. Constraints on the non-thermal population

In order to model the radio emission from IRAS-N and HH 80, and to compute the radiation at high and very high energies, the values of B and $L_{nt}^{e,p}$ for both sources are required. B should be well below B_{eq} (see Eq. 8). The

Table 1. IRAS-N and HH 80 properties and derived parameters (see the text for details)

	IRAS-N	HH 80
n_c [cm ⁻³]	5×10^5	4×10^2
d [kpc]	2.9	1.7
L_* [erg s ⁻¹]	5×10^{38}	8×10^{37}
u [erg cm ⁻³]	2×10^{-9}	2×10^{-12}
Z_j [cm]	5×10^{17}	10^{19}
n_j [cm ⁻³]	5×10^5	4×10^2
R_j [cm]	1.6×10^{16}	5×10^{16}
v_j [cm s ⁻¹]	5×10^7	10^8
v_{bs} [cm s ⁻¹]	5×10^6	5×10^7
v_r [cm s ⁻¹]	5×10^7	5×10^7
t_{life} [s]	10^{11}	3×10^{11}
n_j [cm ⁻³]	5×10^3	4×10^2
χ	0.01	1
L_j [erg s ⁻¹]	5×10^{35}	2×10^{36}

non-thermal luminosity $L_{nt}^{e,p}$ will be taken equal to $0.1 L_s$, or $f_{nt0.1}^{e,p} = 1$. The observed radio fluxes and spectral indices are ~ 8.7 and 3 mJy at 8 GHz and $\alpha \sim 0.5$ and 0.3, respectively (GAR03; MRR93). The value of the index Γ for the radio emitting particles can be obtained from α , as shown in Sect. 5.1. Fixing L_{nt}^e and knowing the radio fluxes, B can be estimated to zeroth order with Eq. (37). We note that equipartition with the relativistic particles would lead to magnetic fields of the order of 0.1-1 mG in the emitting regions (see ARA07 for the case of IRAS-N).

The nature of the radio emitting particles may be primary electrons accelerated in the shock, or secondary e^\pm from pp collisions. If primary electrons dominate the production of the radio emission, the relativistic proton population will be constrained by the fact that secondary radiation cannot overcome that of primary electrons (although pp collisions may still be a significant source of high energy emission). If secondary e^\pm were the origin of the radio emission, the value of Γ for protons should be slightly softer than that of secondary e^\pm (Kelner et al. 2006), and the radio contribution from primary electrons should be minor.

7.2.2. The emission in IRAS-N

Given the values of n_c and v_{bs} in IRAS-N, it seems unlikely that the bow shock is accelerating these electrons. This shock will be strongly radiative, peaking the thermal emission in the optical/UV, with a luminosity of few times 10^{34} erg s⁻¹. On the other hand, the reverse shock is marginally radiative because $l_{cool} \sim R_j$, peaking at 0.5 keV with a bolometric luminosity $\sim 10^{35}$ erg s⁻¹. As mentioned above, the photoelectric absorption τ_X is very large, likely > 100 , implying an almost complete suppression of X-rays, which would explain the non-detection of the source. Concerning the non-thermal radiation, from $f_{nt0.1}^{e,p} = 1$ one obtains $L_{nt}^{e,p} \sim 5 \times 10^{34}$ erg s⁻¹.

If primary electrons produced the radio emission, the magnetic field should be $B \sim 0.1$ mG for the adopted f_{nt} , and the maximum energy, limited by diffusive escape, $E_{max} \sim 4 \times 10^2$ GeV for both electrons and protons. If secondary e^\pm produced the radio emission, $B > 0.5$ mG,

and $E_{\max} > 2 \times 10^3$ GeV (only protons), limited again by diffusive escape.

The density downstream the bow shock may be up to 10^4 times larger than downstream the reverse shock due to strong radiative cooling in the former region. Since t_{RT} should be much shorter than t_{life} , we assume that the RT instabilities have time to develop mixing reverse and bow shock downstream material, effectively increasing the density in the reverse shock. We have adopted a value for F such as that the resulting luminosities due to relativistic Bremsstrahlung and pp collisions be of the order of L_{nt} . In this way, F is used as a free parameter that is optimized to get high gamma-ray luminosities, not to suppress acceleration, and accounting for the constraints given by the observational data at lower energies and the F -limits provided in Sect. 3.2. Following such an approach we have adopted $F \sim 25$. Note that, despite the high density, the Tsyvovich-Razin effect may be neglected, since the entrained dense bow shock material should be cold and hardly fully ionized.

7.2.3. The emission in HH 80

In the case of HH 80, both the reverse and the bow shock are adiabatic. We predict thermal X-rays peaking at ~ 0.5 keV with intrinsic luminosities of the order $\sim (R_j/l_{\text{cool}}) L_s \sim 10^{34}$ erg s $^{-1}$. This value is ~ 100 times bigger than that given by PTM04, where no intrinsic absorption was assumed. However, if an intrinsic $N_{\text{H}} \sim 5 \times 10^{21}$ cm $^{-2}$ in the surroundings of HH 80 were adopted, the factor of 100 could be explained with photoelectric absorption (see the strong dependence of l_{cool} and τ_{X} on photon energy and $v_{\text{r,bs}}$). To compute the non-thermal emission, as noted, the two shocks are treated as just one with $f_{\text{nt},0.1}^{e,p} = 1$, i.e. $L_{\text{nt}}^{e,p} \sim 2 \times 10^{35}$ erg s $^{-1}$.

In the case dominated by primary particles, the magnetic field would be $B \sim 0.005$ mG for the adopted f_{nt} , with a maximum energy limited by diffusive escape $E_{\max} \sim 60$ GeV for both electrons and protons. In the case of dominance by secondaries, $B > 0.02$ mG, and $E_{\max} > 3 \times 10^2$ GeV (only protons), limited again by diffusive escape. Since the medium is quite diluted, relativistic Bremsstrahlung and pp collisions are not as efficient as in IRAS-N, but the fact that $L_{\text{nt}}^{e,p}$ and t_{esc} are both larger renders not so different values for $L_{\text{brems,pp}}$.

7.3. Computed spectral energy distributions

In Figs. 2, 3, 4 and 5, the SEDs computed for IRAS-N and HH 80 are shown. Two scenarios are adopted for both sources, one in which the radio emission is dominated by primary electrons, and another one in which the dominant radio emitters are secondary e^{\pm} . In the former, L_{nt}^e and L_{nt}^p has been taken equal yielding $a \sim 1$; in the latter, we have derived just a lower-limit for a to avoid primary emission to be significant. In IRAS-N, if secondary e^{\pm} were the source of radio emission, a should be > 10 . In HH 80, given the relatively low densities and high magnetic fields of the secondary e^{\pm} scenario, the proton to electron number ratio a should be > 1000 .

It is remarkable that the high-energy components in the SEDs, associated with relativistic Bremsstrahlung and/or pp collisions, have significant luminosities in the high-

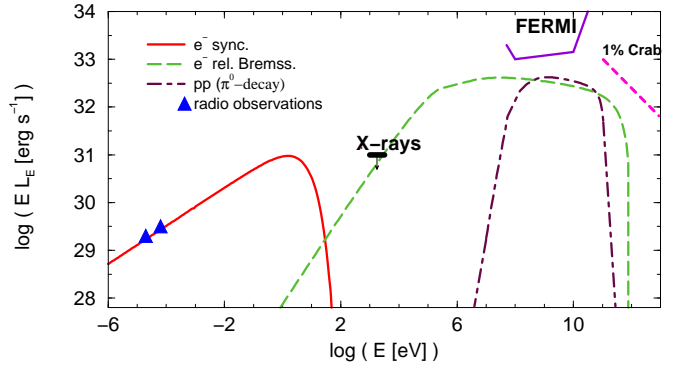


Fig. 2. Spectral energy distribution of the non-thermal emission for IRAS-N in the primary electron scenario. The IC contribution is negligible and not shown here. Observational points are from IRAS 16547–4247 (radio, Rodríguez et al. 2005; X-rays, ARA07). The 1 yr/ 5σ sensitivity of *Fermi* in the direction of the galactic plane is shown. A curve above 100 GeV showing a luminosity corresponding to 0.01 Crab, typical sensitivity of a Cerenkov telescope for exposures of ~ 50 hr, is also presented.

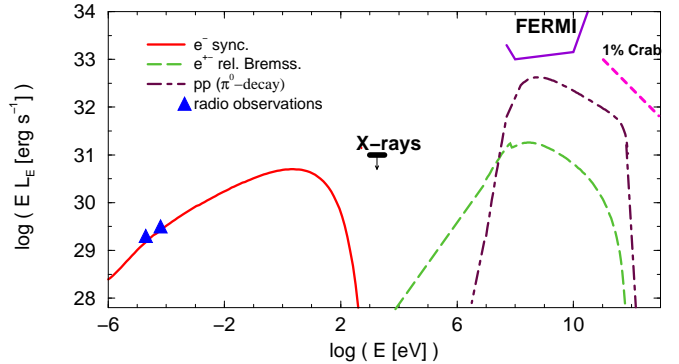


Fig. 3. The same as in Fig. 2 but for the secondary e^{\pm} case.

energy and very high-energy range and fulfill the X-ray constraints. The synchrotron emission peaks in the optical/UV, and can be the dominant cooling channel of electrons only if the magnetic field is rather high and densities low. Interestingly, in the primary electron scenario of HH 80, the electron component does not achieve energies beyond those to emit radio synchrotron emission, but relativistic Bremsstrahlung and pp emission may still be significant at GeV energies.

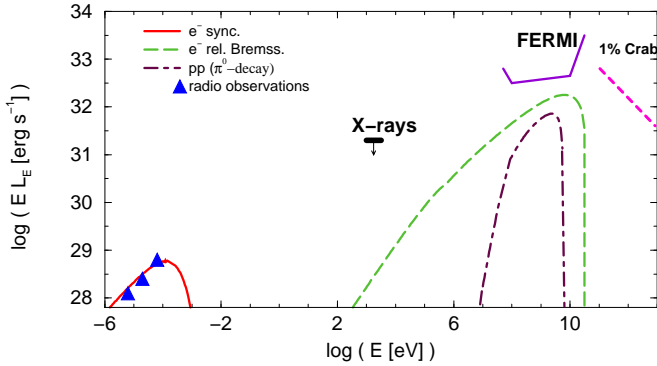
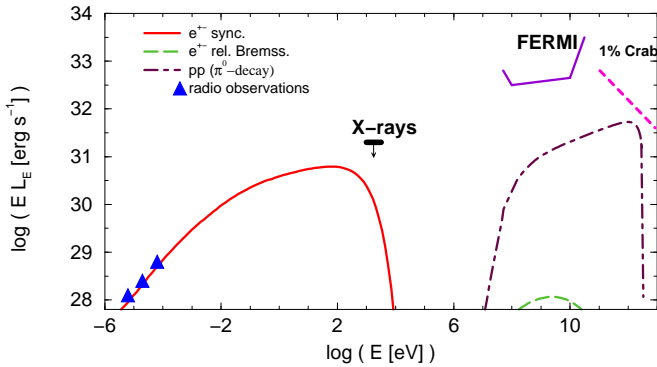
The list of the parameter values adopted to calculate the SEDs, together with the radio properties of the sources, is presented in Table 1. The parameter values have been adjusted numerically and are slightly different from those given in Sect. 7.2.

8. Detectability

The SEDs presented in Figs. 2-5 show that massive YSOs can produce significant amounts of gamma rays, although the results are quite sensitive to the available densities downstream. For sources with high densities like IRAS-N, if the development of RT instabilities does not interfere with particle acceleration, relativistic Bremsstrahlung and pp collisions will be quite efficient. For low-density sources

Table 2. Radio data and parameters of the non-thermal emitter

	IRAS-N		HH 80	
α	0.5		0.3	
F_8 GHz [mJy]	8.7		3	
	primaries ^a	secondaries ^b	primaries	secondaries
a	1	> 10	1	> 1000
n [cm ⁻³]	5×10^5	5×10^5	1.6×10^3	1.6×10^3
t_{esc} [s]	9×10^8	9×10^8	4×10^9	4×10^{11}
$L_{\text{nt}}^{e,p}$ [erg s ⁻¹]	5×10^{34}	5×10^{34}	2×10^{35}	2×10^{35}
B [mG]	0.25	2	0.003	2.5
$E_{\text{max}}(e)$ [GeV]	7×10^2	$\sim 5 \times 10^2$	35	$\sim 10^3$
$E_{\text{max}}(p)$ [GeV]	7×10^2	5×10^3	35	10^4
Γ	2.2	2.4	1.6	1.8

^a Primary electron scenario.^b Secondary e^\pm scenario.**Fig. 4.** The same as in Fig. 2 but for HH 80. Observational points are from Martí et al. (1993) (radio) and PTM04 (X-rays). The X-ray detected point is shown as an upper-limit.**Fig. 5.** The same as in Fig. 3 but for HH 80.

like HH 80, the efficiency of relativistic Bremsstrahlung and pp collisions is lower, but the lobe sizes are expected to be large, increasing the escape timescales and thereby the radiation outcome (see Sect. 5.2). Therefore, for $f_{\text{nt}}^{e,p} \gtrsim 0.1$, it can be expected that the termination regions of massive YSO jets will be eventually detected by Fermi and also by Cherenkov telescopes through long enough exposures.

In our calculations, the magnetic field strength B and $L_{\text{nt}}^{e,p}$ have been adjusted for both to explain the radio fluxes and to obtain significant gamma-ray fluxes. The magnetic field assumed for high-density, IRAS-N-like sources is in

accordance with estimates derived through Zeeman measurements (e.g. Crutcher 1999). In the case of low-density, HH 80-like, sources, the situation may be more complicated.

The primary electron scenario of HH 80 requires a very low magnetic field in the shocked regions. As noted, low densities imply large lobes and therefore lower magnetic fields in the jet head. However, the value of B in the bow shock can hardly be smaller than that in the cloud, which is expected to be, given the cloud densities, several times higher than the one adopted in our calculations. Therefore, in such a scenario and source type, if detected, gamma rays would likely come from the reverse shock. Otherwise, in the secondary e^\pm scenario in HH 80 the magnetic field must be quite high, ~ 2.5 mG, regardless the shock involved, below but close to the maximum value (see Eq. 8). Furthermore, the value for a required in this case, $\gtrsim 1000$, may be too large. Also, the hard particle energy distribution required may be difficult to explain in the context of linear theory of Fermi I particle acceleration. Such a hard radio spectrum may be explained by marginal free-free absorption or by an additional thermal component, but then the expected non-thermal fluxes at higher energies would be smaller due to a softer particle energy distribution. In any case, despite these caveats, one cannot still rule out HH 80 and similar objects as gamma-ray emitters.

It is worth noting that the assumptions adopted in this work are quite conservative. The parameter uncertainties are relatively large, and a more optimistic, but yet consistent with observations, choice of densities, shock velocities and jet luminosities, could easily move the SED curves up by a factor of several.

9. Discussion

Romero (2008) pointed out that the detection of massive protostars at gamma-ray energies would open a new window to star formation studies. The detection of the cutoff in the SED would give important insights on the acceleration efficiency in the terminal shocks of the outflows. The SED can also shed light on the densities, magnetic fields, velocities, and diffusion coefficients in the shocked regions. Although we do not expect that massive protostars should be among the bright sources detected by *Fermi* (Abdo et al. 2009), our calculations show that they could

show up in further analysis of weaker sources after few years of observation. The emission levels above 100 GeV, close to 0.01 Crab, could be detectable by current and future Cherenkov telescopes for observation times moderately longer than 50 hours.

However, not only massive protostars, but also the regions in which they form, may be gamma-ray emitters. As mentioned in Sect. 4, some amount of the highest energy particles may escape to the cloud far upstream the bow shock. It is hard to estimate the fraction of electrons and protons that would be released in the cloud, which depends strongly on the diffusion coefficient of the pre-shock cloud medium and the bow shock velocity and size. However, they might carry a non-negligible fraction of $L_{\text{nt}}^{e,p}$ if $\Gamma \sim 2$. In fact, in the case that $L_{\text{nt}}^{e,p} \sim 0.01 L_j$ were in the cloud, massive YSOs may inject an amount of protons well above the average galactic level at several hundreds of GeV, and the radiation resulting from pp may be detectable (for a general case, see Aharonian & Atoyan 1996), competing with that produced in the lobe itself. For leptons, the emission at high energies may be relevant for low magnetic fields, i.e. when the maximum energy is determined by diffusive escape and dominant relativistic Bremsstrahlung in the cloud. The spectrum of the gamma rays, generated by pp collisions for protons and relativistic Bremsstrahlung for electrons, should be very hard since only the highest energy particles escape, peaking at $\epsilon \lesssim E_{\text{max}}$. The cloud synchrotron emission should be quite diluted and dominated by the lobe.

A clustering of gamma-ray sources should be present in regions with large molecular clouds and star formation, as already inferred from EGRET data (e.g. Romero et al. 1999). The accumulation of cosmic rays accelerated in the radio lobes into the molecular cloud can produce extended gamma-ray sources. These radio lobes may be difficult to detect. Neither UV nor hard X-ray counterparts related to thermal Bremsstrahlung produced in the shock downstream regions are expected to be observed from these sources because of the large absorption and/or low emission levels. Deep inside the cloud, even radio emission may be missing due to strong free-free absorption, so the exact number of accelerators could be hard to estimate. Also, cosmic-ray re-acceleration inside the clouds due to magnetic turbulence (e.g. Dogiel et al. 2004) could result in stronger sources. Therefore, the combined effect of several protostars deeply embedded in giant clouds might be responsible for GeV-TeV sources found in star forming regions by EGRET, *Fermi*, *AGILE* and Cherenkov telescopes. We conclude that massive clouds with high IR luminosities and maser emission (tracers of massive star formation) deserve detailed study with *Fermi* and ground-based Cherenkov telescopes.

Acknowledgements. We thank an anonymous referee for his/her constructive and useful comments that helped to improve the manuscript. V.B.R., G.E.R., and J.M.P. acknowledge support by the Ministerio de Educación y Ciencia (Spain) under grant AYA 2007-68034-C03-01, FEDER funds. V.B.R. wants to thank the Instituto Argentino de Astronomía, and the Facultad de Ciencias Astronómicas y Geofísicas de la Universidad de La Plata, for their kind hospitality. G.E.R. and A.T.A. are supported by CONICET and the Argentine agency ANPCyT (grant BID 1728/OC-AR PICT 2007-00848). A.T.A. thanks Max Planck Institut fuer Kernphysik for kind hospitality and support.

References

Abdo, A.A., et al., 2009, *ApJS*, 183, 46

- Aharonian, F.A., Atoyan, A.M., 1996, *A&A*, 309, 917
 Araudo, A.T., Romero, G.E., Bosch-Ramon, V., Paredes, J. M., 2007, *A&A*, 476, 1289 (ARA07)
 Araudo, A.T., Romero, G.E., Bosch-Ramon, V., Paredes, J. M., 2008, *IJMP D*, 17, 1889 [astro-ph/0805.1898]
 Banerjee, R., Pudritz, R.E., 2006, *ApJ*, 641, 949
 Banerjee, R., Pudritz, R.E., 2007, *ApJ*, 660, 479
 Bell, A.R., 1978, *MNRAS*, 182, 147
 Blondin, J. M., Konigl, A., Fryxell, B. A. 1989, *ApJ*, 337, L37
 Blumenthal, G.R., Gould, R.J., 1970, *Rev. Mod. Phys.*, 42, 237
 Bonnell, I.A., Bate, M.R., Zinnecker, H., 1998, *MNRAS*, 298, 93
 Bordas, P., Bosch-Ramon, V., Paredes, J. M., Perucho, M. 2009, *A&A*, 497, 325
 Crusius-Watzel, A. R. 1990, *ApJ*, 361, L49
 Crutcher, R.M., 1999, *ApJ*, 520, 706
 Dogiel, V.A., Gurevich, A.V., Istomin, Ya. N., Zybin, K.P., 2005, *Ap&SS*, 297, 201
 Drury, L.O'C., 1983, *Reports on Progress in Physics*, 46, 973
 Drury, L.O'C., Duffy, P., Kirk, J. G. 1996, *A&A*, 309, 1002
 Fermi, E., 1949, *Phys. Rev.*, 75, 1169
 Garay, G. & Lizano, S., 1999, *PASP*, 111, 1049
 Garay, G., Brooks, K., Mardones, D., Norris, R.P., 2003, *ApJ*, 537, 739 (GAR03)
 Garay, G., Mardones, D., Bronfman, L., et al. 2007, *A&A*, 463, 217
 Ginzburg, V.L., Syrovatskii, S.I., 1964, *The Origin of Cosmic Rays*, Pergamon Press, New York
 Henriksen, R. N., Mirabel, I. F., Ptuskin, V. S. 1991, *A&A*, 248, 221
 Kaiser, C. R., & Alexander, P. 1997, *MNRAS*, 286, 215
 Kelner, S.R., Aharonian, F.A., & Vugayov, V.V., 2006, *Phys. Rev. D*, 74, 034018
 Lucek, S. G. & Bell, A. R. 2000, *MNRAS*, 314, L65
 Martí, J., Rodríguez, L.F., Reipurth, B., 1993, *ApJ*, 416, 208 (MRR93)
 Martí, J., Rodríguez, L.F., Reipurth, B., 1995, *ApJ*, 449, 184 (MRR95)
 McKee, C.F., Ostriker, E.C., 2007, *ARA&A*, 45, 565
 Morrison, R. & McCammon, D. 1983, *ApJ*, 270, 119
 Myasnikov, A. V., Zhekov, S. A., Belov, N. A. 1998, *MNRAS*, 298, 1021
 Plambeck, R.L. & Menten, K.M., 1990, *ApJ*, 364, 555
 Pravdo, S. H., Tsuboi, Y., Maeda, Y. 2004, *ApJ*, 605, 259 (PTM04)
 Protheroe, R.J., 1999, in: *Topics in Cosmic-Ray Astrophysics*, 1999, p.247 [astro-ph/9812055]
 Rodríguez, L.F., Garay, G., Brooks, K., Mardones, D., 2005, *ApJ* 626, 953
 Reville, B., Kirk, J. G., Duffy, P., O'Sullivan, S. 2007, *A&A*, 475, 435
 Rodríguez, L.F., Moran, J.M., Franco-Hernández, R., et al., 2008, *AJ* 135, 2370 (RMF08)
 Romero, G. E., 2008, in: *High-Energy Gamma-Ray Astronomy*, eds. Aharonian et al., AIP Conf. Proc., Vol. 1085, p. 97
 Romero, G. E., Benaglia, P. & Torres, D. F. 1999, *A&A*, 348, 868
 Rybicki, G. B. & Lightman, A. P. 1979, *Radiative processes in astrophysics* (New York: Wiley-Interscience)
 Seaton, M. J. 1959, *MNRAS*, 119, 81
 Shu, F.H., Adams, F.C., Lizano, S. 1987, *ARA&A*, 25, 23
 Stahler, S. W., Palla, F., Ho, P. T. P., 2000, in: *Protostars and Planets IV*, eds Mannings, V., Boss, A.P., Russell, S. S., University of Arizona Press, Tucson, p. 327